Exploring the role of snow metamorphism on the isotopic composition of the surface snow at EastGRIP

Romilly Harris Stuart[1,4], Anne-Katrine Faber[2], Sonja Wahl[2], Maria Hörhold[3], Sepp Kipfstuhl[3], Kristian Vasskog[4], Melanie Behrens[3], Alexandra Zuhr[5,6], and Hans Christian Steen-Larsen[2]

[1]Laboratoire des Sciences du Climat et de l'Environnement, UMR8212, CNRS – Gif sur Yvette, France
[2]Geophysical Institute, University of Bergen and Bjerknes Centre for Climate Research, Bergen, Norway
[3]Alfred-Wegener-Institut Helmholtz-Zentrum für Polar- und Meeresforschung, Bremerhaven, Germany
[4]Department of Geography, University of Bergen, and Bjerknes Centre for Climate Research, Bergen, Norway
[5]Alfred-Wegener-Institut Helmholtz Zentrum für Polar- und Meeresforschung, Research Unit Potsdam, Telegrafenberg A45, 14473 Potsdam, Germany
[6]University of Potsdam, Institute of Geosciences, Karl-Liebknecht-Str. 24-25, 14476 Potsdam-Golm, Germany

Correspondence: Romilly Harris Stuart (romilly.harris-stuart@lsce.ipsl.fr)

Abstract.

Stable water isotopes from polar ice cores are invaluable high-resolution climate proxy records. Recent studies have aimed to improve understanding of how the climate signal is stored in the stable water isotope record by addressing the influence of post-depositional processes on the surface snow isotopic composition. In this study, the relationship between surface snow metamorphism and water isotopes during precipitation-free periods is explored using measurements of snow specific surface area (SSA). Continuous daily SSA measurements from the East Greenland Ice Core Project site (EastGRIP) situated in the accumulation zone of the Greenland Ice Sheet during the summer seasons of 2017, 2018 and 2019, are used to develop an empirical decay model to describe events of rapid decrease in SSA, linked to snow metamorphism. We find that SSA decay during precipitation-free periods at EastGRIP is best described by the exponential equation $SSA(t) = (SSA_0 - 22) \cdot e^{-\alpha t} + 22$, and has a dependency on temperature and wind-speed. The relationship between surface snow SSA and snow isotopic composition is primarily explored using Empirical Orthogonal Function analysis. A coherence between SSA and d-excess is apparent during 2017 and 2019, suggesting that processes driving change in SSA also influence snow isotopic composition. In contrast, 2018 was characterised by a covariance between SSA and δ^{18}O highlighting the inter-annual variability in surface regimes. Moreover, we observed changes in isotopic composition consistent with fractionation effects associated with sublimation and vapour diffusion during periods of rapid decrease in SSA. Our findings support recent studies which provide evidence of isotopic fractionation during sublimation.

1 Introduction

The traditional interpretation of stable water isotopes in ice cores is based on the linear relationship between local temperature and first-order parameters δ^{18}O and δD of surface snow on ice sheets (Dansgaard, 1964). Accurate reconstruction requires consideration of precipitation intermittency (Casado et al., 2020; Laepple et al., 2018), past variations in ice-sheet elevation

(Vinther et al., 2009), sea ice extent (Faber et al., 2017; Sime et al., 2013), and firn diffusion (Johnsen et al., 2000; Landais et al., 2006; Holme et al., 2018), which influence the water isotopic composition in ice cores. The second-order parameter deuterium excess (d-excess) is defined by the deviation from the near-linear relationship between δ^{18}O and δD which is driven by non-equilibrium (kinetic) fractionation (d-excess$= \delta$D$ - 8 \cdot \delta^{18}$O). d-excess in ice cores is understood to reflect moisture source conditions (Dansgaard, 1964; Merlivat and Jouzel, 1979; Johnsen et al., 1989), changes in moisture source region (Masson-Delmotte et al., 2005), and can be modified during snow crystal formation in supersaturated clouds (Ciais and Jouzel, 1994; Sodemann et al., 2008).

Recent studies have documented isotopic composition change in the surface snow during precipitation-free periods (Steen-Larsen et al., 2014; Ritter et al., 2016; Casado et al., 2018; Hughes et al., 2021), linked to synoptic variations in atmospheric water vapour composition and subsequent exchange with the surface snow (Steen-Larsen et al., 2014; Ritter et al., 2016; Madsen et al., 2019; Hughes et al., 2021; Wahl et al., 2021; Casado et al., 2021). Post-depositional processes at the surface involve additional kinetic effects adding complexity to the interpretation of d-excess (Hughes et al., 2021; Casado et al., 2021). Here we focus on processes influencing isotopic composition of the surface snow after deposition while exposed to surface processes and concentrate on the second order parameter d-excess.

After deposition, snow grains undergo structural changes known as snow metamorphism, which is active at the surface and at greater depths, depending on temperature (gradient) conditions (Colbeck, 1983; Pinzer and Schneebeli, 2009). Surface snow metamorphism is initially driven by a reduction in the snow-air interface to reach thermodynamic stability (Colbeck, 1980; Legagneux and Domine, 2005). The snow-air interface can be described by the widely used parameter snow specific surface area (SSA), which is dependent on optical grain radius and density of ice ($SSA = 3/\rho_{ice} \cdot r_{opt}$) (Gallet et al., 2009), and can be used as a measure for snow metamorphism (Cabanes et al., 2002, 2003; Legagneux et al., 2002). Freshly deposited snow has a high SSA which decreases with time under both isothermal (<10 °C m^{-1}) and temperature gradient (>10 °C m^{-1}) conditions within the snow (Cabanes et al., 2002; Legagneux et al., 2004; Domine et al., 2007; Genthon et al., 2017). Decrease in SSA is predominantly the result of Ostwald Ripening, where large grains grow at the cost of smaller grains (Lifshitz and Slyozov,1961; Legegneux et al., 2004), interstitial vapour diffusion (Flin and Brzoska, 2008; Sokratov and Golubev, 2009; Pinzer et al., 2012), and wind effects (Picard et al., 2019). Under natural conditions, SSA decrease is driven by a combination of these processes depending on surface conditions (Cabanes et al., 2003; Pinzer and Schneebeli, 2009), each potentially modifying the isotopic composition of the snow (Ebner et al., 2017).

Models can provide a quantitative description of SSA decrease after deposition. Previous studies have proposed SSA decay models using a combination of field measurements and controlled laboratory experiments (Cabanes et al., 2002, 2003; Legagneux et al., 2003, 2004; Flanner and Zender, 2006; Taillandier et al., 2007). Exponential models are documented to produce the best fit to in-situ SSA decay data (Cabanes et al., 2003). A subsequent physical-based model was defined by Legagneux et al. (2003) to describe SSA decay based on grain growth theory, which was then further developed by Flanner and Zender (2006), who defined parameters based on surface temperature, temperature gradient and snow density. Existing SSA decay models have rarely been applied to polar ice sheet surface snow (Linow et al., 2012; Carmagnola et al., 2013). Conditions for surface snow on polar ice sheets are not necessarily comparable to other alpine and Arctic regions due to negligible melt and

the high-latitude radiation budget. Moreover, while continuous surface SSA measurements exist from Antarctica (Gallet et al., 2011, 2014; Picard et al., 2014), those from Greenland focus on the depth evolution of SSA (Carmagnola et al., 2013; Linow et al., 2012). Continuous datasets of daily SSA and corresponding isotopic composition measurements from the accumulation zone of the Greenland Ice Sheet can contribute to understanding the relevance of snow metamorphism for surface energy budget and for ice core studies. The latter is of particular interest owing to observations of isotopic fractionation during snow metamorphism documented in laboratory studies (Ebner et al., 2017) and field experiments (Hughes et al., 2021; Wahl et al., 2021; Casado et al., 2021). Nonetheless, few studies have focused on the direct relationship between physical snow properties, such as SSA, and post-depositional changes in isotopic composition.

In this manuscript, the aim is to explore the behaviour of surface snow metamorphism on polar ice sheets using daily SSA measurements from Northeast Greenland during summer, and to compare the change in physical properties to the isotopic composition measurements. The primary focus is to document events where changes in SSA occur rapidly over a number of precipitation-free days, which we use as a proxy for snow metamorphism. Events of rapid SSA decrease (SSA decay events) are used to 1) quantify and model surface snow metamorphism in polar snow and, 2) assess isotopic change during surface snow metamorphism in-situ. The data presented here has great value for our understanding of the influence of post-depositional processes on physical and isotopic changes in the polar ice sheet surface snow. This allows for deeper understanding of snow properties at remote regions of polar ice sheets and contributes to the interpretation of water isotopes in polar ice cores.

2 Study site and methods

2.1 EastGRIP site overview and meteorological data

All data used in this paper was collected as part of the Surface Program corresponding to the international deep ice core drilling project at the East Greenland Ice Core Project site (EastGRIP 75.65°N, 35.99°W; 2,700 m.a.s.l) during summer field seasons (May - August) of 2017, 2018 and 2019. The local accumulation rate is approximately 14 cm water equivalent per year (Schaller et al., 2017).

Meteorological data used for this study are from the Program for Monitoring of the Greenland Ice Sheet (PROMICE) Automatic Weather Station set up by the Geological Survey of Denmark and Greenland (GEUS) at EastGRIP in 2016 (Fausto et al., 2021). The data are 10-minute mean values for a number of variables. In addition to the surface variables, snow temperature was measured using a thermistor string at 0.1 m intervals during 2017 and 2018 but was modified to 1 m intervals in 2019. An additional thermistor string was thus installed in May of 2019, from which we use the 0.1 m measurements. Relevant weather variables for this study are surface temperature (calculated from longwave radiation down and longwave radiation up with longwave emissivity set at 0.97), air temperature and wind speed (Van As, 2011). Mean weather conditions vary between sampling years, as outlined in Table 1 with prevailing westerly winds throughout the sampling seasons.

An eddy-covariance (EC) measurement tower was set up at EastGRIP for every summer observation period (Madsen et al., 2019; Wahl et al., 2021). Here we use the 30-minute latent heat flux (LE) measurements which are calculated from the measurement of humidity fluxes between the surface and atmosphere. Positive LE indicates upwards energy flux in the form of

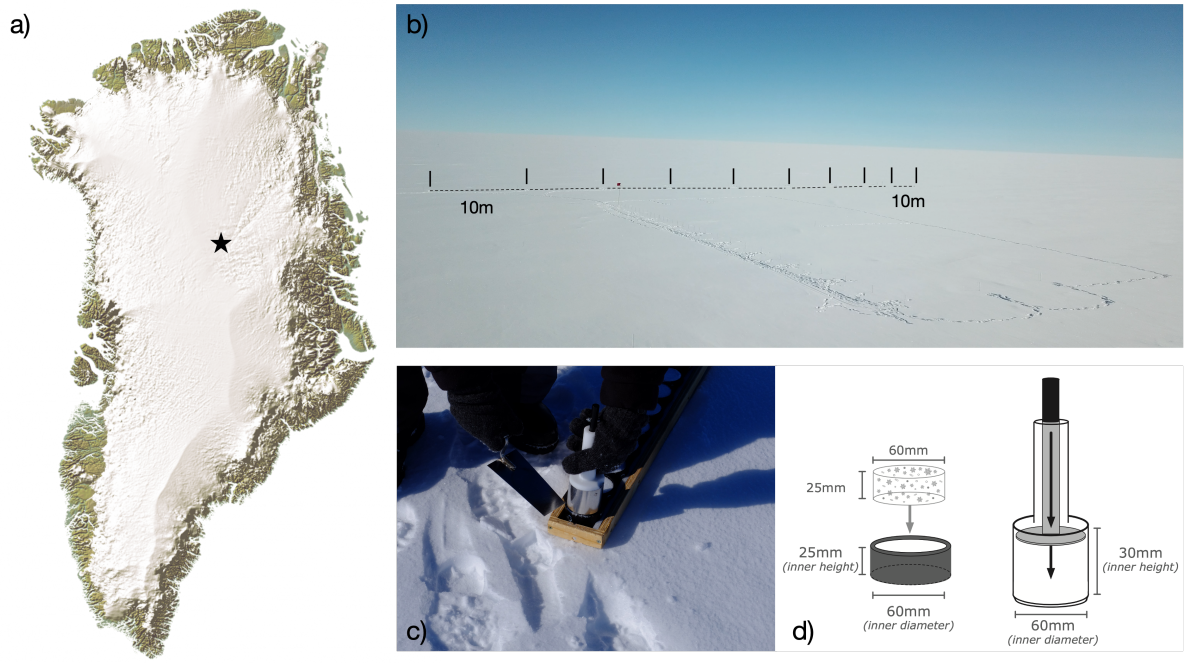

Figure 1. a) A map of Greenland with a black star indicating the EastGRIP site (Source: VisitGreenland). b) A photograph of the clean snow area at the field site (Credit: Bruce Vaughn), black lines indicate the SSA sampling transect with 10 m spacing shown as dashed lines. c) A photograph of SSA sampling cups (Credit: Sonja Wahl), and d) an illustration of the sampling device from Klein (2014).

sublimation in Table 1. Significant weather conditions such as ground fog, drifting snow and snowfall, were documented each day in the EastGRIP field diary.

Table 1. Weather statistics - 2017, 2018 and 2019. Mean and standard deviation for weather variables during the three sampling seasons. Surface temperature, relative humidity with reference to ice and wind speed use PROMICE weather station based on 10-minute measurements. Latent heat flux a 30-minute mean upwards flux from the eddy-covariance tower.

		2017	**2018**	**2019**
	Instrument	*06/05 - 05/08*	*04/05 - 07/08*	*24/05 - 01/08*
Surface Temperature (°C)	(Kipp and Zonen CNR1/CNR4 radiometer)	-14.5 ± 6.2	-15.76 ± 7.6	-10.6 ± 5.4
Relative Humidity (%)	(Calculated)	95.8 ± 15	95.9 ± 16	93.3 ± 14
Wind Speed ($\mathrm{m\,s^{-1}}$)	(R.M. Young 05103-5 $\pm 0.3\,\mathrm{m\,s^{-1}}$)	4.9 ± 0.2	4.2 ± 1.9	4.5 ± 1.6
Latent Heat Flux ($\mathrm{W\,m^{-2}}$)	(IRGASON Campbell Scientific)	1.28 ± 4.2	1.3 ± 4.3	2.6 ± 5.2

2.2 Snow sampling procedure and snow accumulation

Each summer season of 2017, 2018 and 2019 snow samples were taken once a day, primarily in the morning, from May to August at 10 sampling sites. Each site was marked by a stick, along a 90 m transect with 10 m spacing upwind of the EastGRIP camp to ensure clean snow (Fig. 1b). The specific dates for each season are given in Table 1. The precise location of each sample was marked by a small stick to ensure the adjacent snow is sampled the next day and to avoid sampling snow from different depths. A 6 cm diameter sampling device collected the top 2.5 cm of surface snow (Fig. 1c). Snow density is determined using the weight of each snow sample with a known volume. Sticks were placed at each sampling site at the start of each season to measure snow height, that is, the distance between the snow surface and top of the stick with a ruler with an uncertainty margin of ± 0.5 cm. Accumulation, used here to describe the change in snow height (cm), was calculated using the cumulative sum of the daily difference between measurements of snow height from each site. The resultant datasets consist of 10 daily measurements of three parameters, SSA, density and snow accumulation. The field season for 2018 started on the 5th of May, 9-days earlier than 2017 (14th May), and 22 days earlier than 2019 (27th May). The meteorological data is re-sampled to the SSA sampling time-periods to ensure consistent comparison.

2.3 SSA measurements

Each snow sample is placed into the Ice Cube sampling container below an Infra-Red (IR) laser diode (1310 nm), where the SSA is calculated based on IR hemispherical reflectance, as explained in Gallet et al. (2009). More information on the Ice Cube device can be found in Zuanon (2013). The *e*-folding depth of 1310 nm radiation in snow of 200 kg m^{-3} is approximately 1 cm (Gallet et al., 2009). Thus, as the mean snow density from all field seasons is 293 kg m^{-3} (307 ± 40 kg m^{-3}, 278 ± 47 kg m^{-3}, 294 ± 50 kg m^{-3} for 2017, 2018 and 2019), each measurement will be heavily weighted towards the top <1 cm of the 2.5 cm sample. The light reflected from the snow samples is converted into inter-hemispheric IR reflectance using a calibration curve based on methane absorption methods (Gallet et al., 2009). A radiative-transfer model is used to retrieve SSA from inter-hemispherical IR reflectance. To avoid influence from solar radiation, SSA was measured inside a white tent or in a snow cave kept at temperatures between -5 °C and -20 °C. We assume an uncertainty of 10% for SSA measurements between 5–130 m^2 kg^{-1} (Gallet et al., 2009).

2.4 Surface snow isotopes

Individual SSA samples were put in separate bags and subsequently measured for water isotopic composition. Thus, every day the 10 SSA samples have a corresponding isotopic composition. The resultant isotope value is the average composition over the top 2.5 cm of snow. Each sample was kept frozen during transportation and storage. The samples were then analysed at Alfred Wegener Institute in Bremerhaven using a cavity ring-down spectroscopy instrument (Picarro L-2120-i and L-2140-i) following the protocol of Van Geldern and Barth (2012). This technique produces δ^{18}O and δD measurements with an uncertainty of 0.15‰ and 0.8‰ respectively. The calculated values for *d*-excess have an uncertainty of 1‰.

2.5 Data analysis

2.5.1 Defining SSA decay events

Freshly deposited snow has a high SSA that slowly decreases through time due to snow metamorphism. Based on this understanding, two terms are defined: 1) SSA increase indicating deposition events in the form of precipitation, drifted snow or surface hoar formation, and 2) SSA decay due to snow metamorphism and other post-depositional processes such as wind-erosion, where the SSA decreases. Identification of such SSA decays in the time-series are required to quantify snow metamorphism and corresponding isotopic change during precipitation-free periods. Surface conditions are subsequently assessed to remove events where the surface snow layer is likely to have experienced perturbation via deposition or erosion.

A threshold is derived to systematically identify periods of rapid SSA decay - hereafter referred to as SSA decay events - over a two-day period which was found to be the most representative time step to capture SSA decay events for all sampling years. SSA decay events captured by this threshold are defined by the peak SSA value (day-0), through to the next increase in SSA (rather than decrease).

A set of criteria are required to reduce the potential of analysing SSA decay events with wind-perturbed surfaces. In Antarctica, unconsolidated surface snow has been observed to drift at wind speeds as low as $5\,\mathrm{m\,s^{-1}}$ measured at 2 m height (Birnbaum et al., 2010). However, a study from north-east Greenland documented snowdrift starting at $6\,\mathrm{m\,s^{-1}}$ (Christiansen, 2001), due to warmer temperatures facilitating bonding of the surface snow (Li and Pomeroy, 1997). Field-diary observations from EastGRIP document snowdrift when wind speeds exceeded $7\,\mathrm{m\,s^{-1}}$.

Based on this assessment, we define two wind-speed categories for comparison of the effects of wind-speed on SSA decay. The first includes events with daily maximum wind-speed below $6\,\mathrm{m\,s^{-1}}$, hereafter referred to as low-wind events, with negligible surface perturbation. Secondly, we consider events where the daily maximum wind-speed is between 6–$7\,\mathrm{m\,s^{-1}}$, hereafter referred to as the moderate-wind events. The inclusion of moderate-wind events facilitates an assessment of the influence of wind-speed on SSA decay, while the threshold wind-speed for snowdrift based on temperature conditions from Li and Pomeroy (1997) is used to ensure minimal chance of drift.

2.5.2 Modelling surface snow metamorphism

The first empirical SSA decay model, Eq.(1), was proposed by Cabanes et al. (2003) who described a temperature-dependent exponential decay based on snow samples collected from the Alps (Cabanes et al., 2002) and Arctic Canada (Cabanes et al., 2003). Legagneux et al. (2003) found Eq.(2) to best describe experimental SSA decay under controlled laboratory conditions.

$$SSA(t) = SSA_0 \cdot e^{-\alpha t} \tag{1}$$

$$SSA(t) = B - A \cdot ln(t + \Delta t) \tag{2}$$

Parameters A and B in Eq.(2) were found to be arbitrarily related to the decay rate and initial SSA of each sample. To improve the physical basis of the model, the theory of Ostwald Ripening, describing grain growth driven by thermodynamic instability, was implemented into the model (Legagneux et al., 2004). Eq. (3) has two parameters τ and n; τ is the decay rate and n relates to theoretical grain growth. The physical model was further developed by Flanner and Zender (2006) to incorporate a physical quantification of the parameters including information about temperature, temperature gradient, and density. Based on these three conditions, they created a look-up table for τ and n.

$$SSA(t) = SSA_0 \cdot \left(\frac{\tau}{t+\tau}\right)^{1/n} \tag{3}$$

Taillandier et al. (2007) proposed two equations based on Eq. (2) to define the decay rate under isothermal and temperature gradient conditions where they were able to directly incorporate a surface temperature parameter (T_m).

$$SSA(t) = [0.659 \cdot SSA_0 - 27.2 \cdot (T_m - 2.03)] - [0.0961 \cdot SSA_0 - 3.44 \cdot (T_m - 1.90)] \cdot (t + e^{\left(\frac{0.659 \cdot SSA_0 - 27.2 \cdot (T_m - 2.03)}{[0.0961 \cdot SSA_0 - 3.44 \cdot (T_m - 1.90)]}\right)}) \tag{4}$$

Building upon previous studies, we define an empirical SSA decay model using continuous daily SSA measurements from EastGRIP to describe the behaviour of surface snow SSA in polar summer conditions (Cabanes et al., 2002, 2003; Flanner and Zender, 2006; Legagneux et al., 2002, 2003; Taillandier et al., 2007). A recent study at EastGRIP has shown the significant heterogeneity in surface snow due to post-depositional reworking from the wind (Zuhr et al., 2021), and therefore each sample is treated individually to avoid signal attenuation.

3 Results

3.1 EastGRIP meteorological conditions

Meteorological variables over the three sampling seasons vary substantially as shown in Fig. 2. Air temperatures were below -30 °C between May 5th and May 8th in 2018. Such low temperatures were not recorded for 2017 and 2019. Moreover, when comparing the period from May 27th to August 5th of each year (duration of 2019 season), 2018 air temperatures (-13.3 °C) were still 0.5 °C lower than 2017 and 3.2 °C lower than 2019.

The 2017 season was characterised by high wind intrusions of $>13\,\mathrm{m\,s^{-1}}$ at approximately 20-day intervals. Considering all three sampling years, the average daily maximum wind speed is $7\,\mathrm{m\,s^{-1}}$, with 209 out of the total 237 sampling days having maximum wind speed above $5\,\mathrm{m\,s^{-1}}$. The distributions of daily maximum wind-speed compared to 10-minute mean values are found in the Supplemental Fig. A1. Between the start and end of the 2017 field season, we observed net-accumulation of 4.81 cm of snow over the 89-day season, compared to 9.30 cm in 2018 and 8.58 cm in 2019. In addition, the total sum of LE during 2019 was 30% greater than in 2018 indicating strong sublimation. Eddy-covariance LE measurements are supported by LE from AWS observations which indicate the same magnitude of difference between the years.

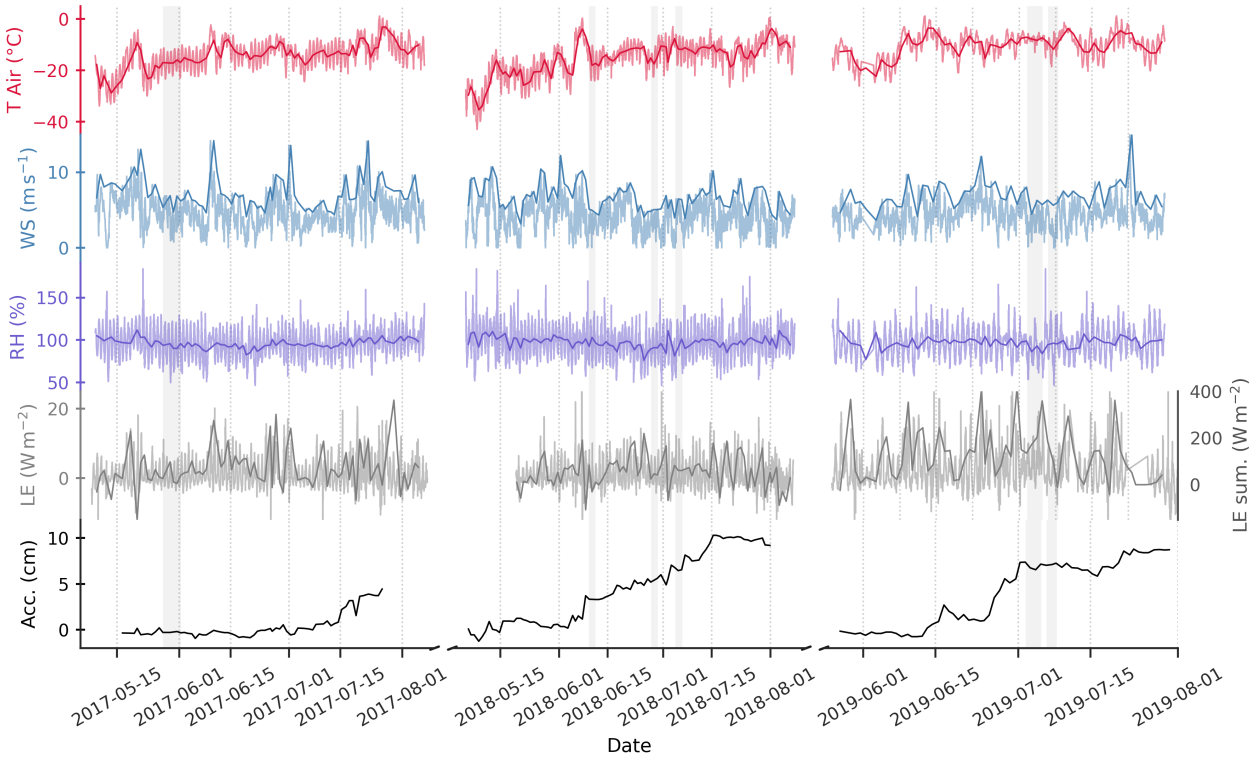

Figure 2. Time series of the ambient conditions during the sampling periods. Data covers the specific sampling periods each year. 10-minute mean data from the AWS is presented for air temperature, wind-speed and relative humidity. Mean values (bold lines) are shown for air temperature and relative humidity, while daily maximum is shown for wind-speed. Latent heat flux data are 30-minute averages from the eddy-covariance tower, with the daily sum shown in bold. Snow accumulation is presented in the lower panel as the daily mean over the 10 sampling sites (see Section 2.2). Grey bars indicate the derived SSA decay events.

3.1.1 Spatial and temporal snow surface variability

Seasonal variability is observed in SSA, δ^{18}O and d-excess throughout the field seasons of 2017, 2018 and 2019 (Fig.3), with highest daily spatial variability in isotopic composition. SSA is characterised by peaks, often corresponding to high spatial variability, followed by gradual decreases over a number of days, the SSA decay feature which is most prominent during 2017 and corresponds to negligible or decreasing accumulation. High SSA values at the start of the 2018 season (daily mean 88 m^2 kg^{-1}) correspond to low and spatially homogeneous δ^{18}O.

Inter-annual difference is observed in δ^{18}O, with seasonal mean values of -31.6$\pm$2.1‰, -32.7$\pm$1.3‰ and -27.3$\pm$2.1‰ for 2017, 2018 and 2019 respectively (Fig. 3). Throughout the season δ^{18}O follows a gradual increasing trend from May to August following increasing temperatures. Note that the 2019 field season started approximately 15 days later than 2017 and 2018, resulting in a bias towards mid-summer conditions. Cases of abrupt decreases (-10‰) are observed in the late summer,

for example, on July 12th in 2018 and July 25th in 2019, which correspond to late-summer snowfall events. No clear seasonal trend is observed in *d*-excess, but rather there are periods of gradual decrease in *d*-excess during periods with no accumulation in all years. The most apparent is from May 15th to June 14th in 2017 corresponding to 0 cm net-accumulation (Fig. 3). The maximum daily spread in δ^{18}O and *d*-excess is approximately 15‰, indicating strong surface heterogeneity.

Empirical Orthogonal Function (EOF) analysis is applied to the data to identify the dominant modes of variance in both the temporal and spatial dimensions for each parameter - SSA, δ^{18}O and *d*-excess. Using a confidence interval of 95% ($p<0.05$), the relationship between SSA and isotopic composition is tested. The spatial and temporal principal components returned for each variable by the EOF are presented in Fig. 3. During 2017, 2018 and 2019 all variables have one dominant mode of variance, or principal component (PC1). PC1 of SSA ($PC1_{SSA}$) explains 61 %, 77 % and 72 % of variance for the respective years, PC1 of δ^{18}O ($PC1_{\delta^{18}O}$) explains 69 %, 83 % and 75 % of the total variance respectively, while PC1 of *d*-excess ($PC1_{dxs}$) explains 47 %, 51 % and 60 %.

Results from the EOF analysis reveals distinct differences between the sampling years, most prevalent is the opposing regime from 2018 to 2019. During 2018, $PC1_{\delta^{18}O}$ and $PC1_{dxs}$ have an inverse correlation in the spatial dimension ($r=-0.6$), and a significant positive correlation between $PC1_{\delta^{18}O}$ and $PC1_{dssa}$ in the temporal dimension ($p<0.05$, $r=0.5$) (Fig. A2 and Fig.

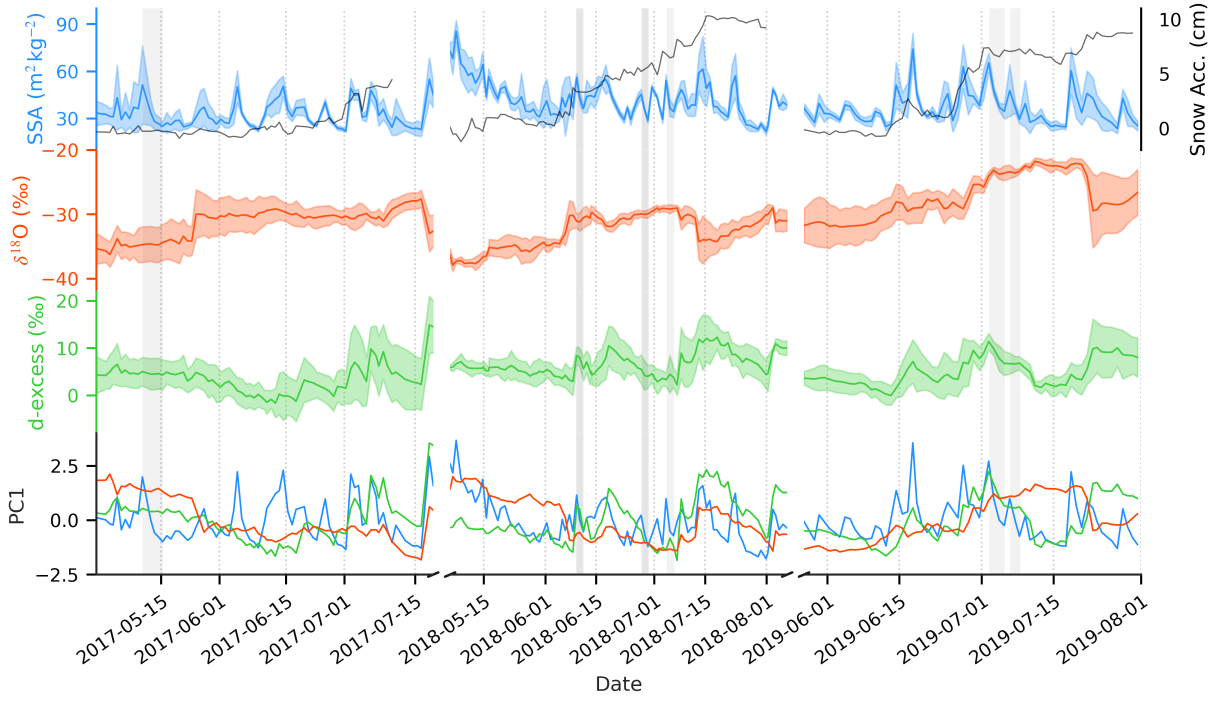

Figure 3. Time-series of SSA (blue), d18O (orange), *d*-excess (green) and the first principal components (PC1) of each variable in the lower panel. Bands in the upper three panels show spatial standard deviation between the 10 sampling sites. The secondary y-axis in the top panel shows the average snow accumulation. The grey bars indicate the SSA decay events.

A3). In contrast, data from 2019 are characterised by significant positive correlations between $PC1_{SSA}$ and of $PC1_{dxs}$ in both the spatial ($p<0.05$, $r=0.75$) and temporal dimensions ($r=0.3$, $p>0.05$), while no relationship is observed between $PC1_{\delta^{18}O}$ and $PC1_{dxs}$. During 2017, there is a weak positive correlation the temporal component of $PC1_{SSA}$ and $PC1_{dxs}$ ($p<0.05$, $r=0.3$), and the temporal $PC1_{\delta^{18}O}$ and $PC1_{dxs}$ ($p<0.05$, $r=0.4$). There is an apparent shift after July 15th where $PC1_{dxs}$ transitions from co-varying with $PC1_{\delta^{18}O}$ to co-varying with $PC1_{SSA}$. Figure A2 and Fig. A3 in the supplement illustrate the spatial and temporal components of the EOF results.

3.2 SSA decay events

3.2.1 Observations

In agreement with Eq. (1), we observe a relationship between initial SSA and subsequent magnitude of decrease when evaluating the SSA decay events (Fig 3). From the years 2017, 2018 and 2019 a total of 21 events are identified that fulfill the SSA decay criteria (as defined in Section 2.5.1). These events are named E1, E2 etc (Table A).

Prior to analysis, we assess the meteorological conditions and field observations to remove SSA decay events with potentially perturbed surface snow. This includes all events coinciding with observations of ground fog, snowdrift, and snowfall, and events where the wind-speed exceeds the thresholds defined in Section 2.5.1. Out of 21 events captured by the SSA decay event threshold, 15 are influenced by either snowdrift, snowfall, or ground fog according to field diary observations, or high wind-speeds (maximum wind-speed $>7\,\mathrm{m\,s^{-1}}$). Of the remaining 6 events, two are in the low-wind category (E10 and E11 $=5.1\,\mathrm{m\,s^{-1}}$), and 4 in the moderate-wind category. Both E10 and E11 had consistent clear sky conditions. Note that E11 was preceded by significant ground fog, not snowfall, indicating that the peak value of $46\,\mathrm{m^2\,kg^{-1}}$ was likely the result of surface hoar, and thus, rapid SSA decay follows an SSA peak not caused by precipitation.

The rate of SSA decay is strongly influenced by the initial SSA during the decay period (Fig. 4), showing that the rate of change is proportional to the absolute value, as described by an exponential decay law ($r=-0.71$ and $r=-0.91$ for low- and moderate-wind events respectively). The mean air temperature for all SSA decay events was between -17.3 °C and -7 °C. The first day of each event is characterised by the largest change in SSA, followed by a decrease in magnitude over the subsequent days, with negligible change in SSA below $22\,\mathrm{m^2\,kg^{-1}}$.

3.2.2 Model

SSA decay rate is quantified by plotting the rate of change in SSA per day against the absolute SSA value for all 10 sampling sites for low- and moderate-wind events (Fig. 4a). We observe a linear relationship between the change in SSA from one day to the next (ΔSSA) and SSA.

The SSA decay model for EastGRIP is constructed using the differential equation for the linear relationship between ΔSSA and absolute SSA. Solving the differential with respect to time (t), produces the SSA decay model defined as Eq. (5), which follows the equation structure of Eq. (1).

$$SSA(t) = (SSA_0 - 22) \cdot e^{-\alpha \cdot t} + 22 \tag{5}$$

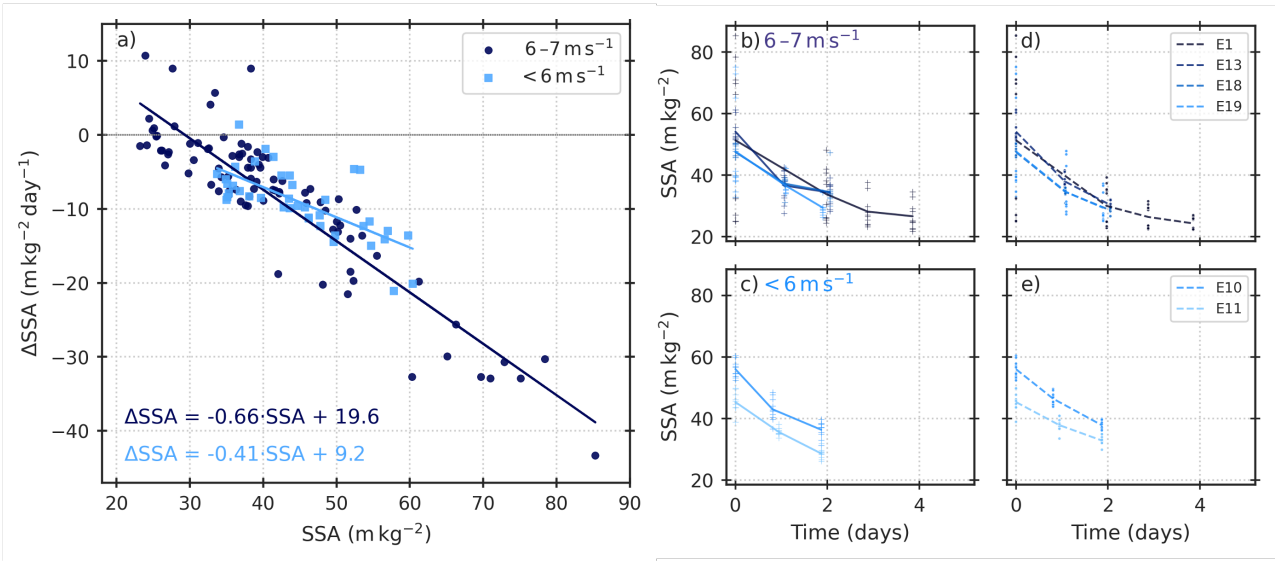

Figure 4. Linear regressions for change in SSA against the SSA for the low-wind (light-blue) and moderate-wind (dark-blue) SSA decay events (a) considering all individual samples. The observed SSA decays are shown for the moderate-wind events (b), and the low wind events (c), followed by the modelled SSA decays for the respective events in d) and c). The legend in d) and e) corresponds to SSA decay event number in Table A

Where SSA(t) is the SSA measurement at a given time in days since the first measurement (initial SSA), SSA_0 is the initial SSA value, α is the decay rate, and a decay constant of 22 $m^2\,kg^{-1}$ is defined for both equations by the minimum SSA value where the derivative of SSA is equal to 0 $m^2\,kg^{-1}$. The decay rate, determined by the slope of the linear regressions in Fig. 4, is higher for moderate-wind SSA decay events (-0.66 $m^2\,kg^{-1}\,day^{-1}$) than for low-wind SSA decay events (-0.41 $m^2\,kg^{-1}\,day^{-1}$). Within the temperature range of low- and moderate-wind SSA decay events from this study, there is no observable temperature dependence of the SSA decay rate. However, such a temperature dependence is clear in events which were excluded due to potential surface perturbations, where there is a decrease in decay rate and increase in the background SSA value with low temperatures (Fig. A4). Our results indicate a slower rate of decay under decreased wind-speed conditions.

3.2.3 Model performance

Model performance is tested by comparing daily predicted decrease to the 10 daily observations, and by comparing model predictions from this study to those from Flanner and Zender (2006) hereafter referred to as FZ06, and the model defined by Taillandier et al. (2007), hereafter T07, as defined in Section 2.5.2. Residuals between our model and the observations are normally distributed, suggesting no systematic errors in model predictions. The root mean squared error (RMSE) between our model predictions and observed mean SSA is 2.48 $m^2\,kg^{-1}$ and 2.60 $m^2\,kg^{-1}$ for the low-wind and moderate-wind SSA decay events respectively.

Table 2. RMSE values for model evaluation. This Study uses the respective α for the low- and moderate-wind events for daily (mean) and individual samples. FZ06 parameters τ and n are defined from the look-up table in Flanner and Zender (2006). T07 uses the mean surface temperature for each event as an input parameter.

	Low-wind		**Moderate-wind**	
	Mean	Individual	Mean	Individual
	$m^2\,kg^{-1}$	$m^2\,kg^{-1}$	$m^2\,kg^{-1}$	$m^2\,kg^{-1}$
This Study	2.48	3.50	2.60	4.28
FZ06	6.46	6.90	7.90	9.52
T07	5.63	6.10	5.27	6.49

Parameter values for τ and n in FZ06 are defined for each event based on mean density, surface temperature and temperature gradient using the extensive look-up table referenced in Flanner and Zender (2006). FZ06 consistently overestimates the SSA decay rate, with residuals increasing throughout the events (See Fig. A5). T07 is able to accurately predict the moderate-wind events, with largest errors associated with E1, the event featuring the lowest temperatures and highest wind-speeds. which has relatively lowest temperatures and highest wind-speeds. However, for low-wind events T07 consistently underestimates the SSA decay rate. RMSE values presented in Table 2 indicate that the model from this study predicts decay with the least error, for both wind-speed categories.

3.3 Isotopic change during SSA decay events

3.3.1 Low- and moderate-wind event analysis

EOF analysis in Section 3.1.1 indicates a relationship between SSA and isotopic composition, most pronounced in 2019. With the understanding that decreasing SSA for low- and moderate-wind events is the result of snow metamorphism of an unperturbed snow surface, we can now document concurrent isotopic changes in the snow. For both low- and moderate-wind events, rate of change in *d*-excess is plotted against the rate of change in SSA (Fig. 5), after the first and second day of each event. We here include analysis of the change in *d*-excess after the second day (referred to as a 2-day change), presented in Table 3 for each low- and moderate-wind events.

Both δ^{18}O and *d*-excess change from the initial value (day-0) in all events, with the percentage change in *d*-excess being the same order of magnitude as for SSA, and an order of magnitude higher than that of δ^{18}O. Three out of six events are characterised by increasing δ^{18}O and decreasing *d*-excess after 2-days. E1, E13 and E19 deviate from this pattern. E13 and E19 both correspond to total increase in δ^{18}O and *d*-excess, whereas E11 is characterised by a slight decrease in δ^{18}O and decrease in *d*-excess (Table 3). The Δd-excess over 1-day indicates a slight negative skew around a mean of -0.3‰. 4 of 6 events (61% of all sample sites) experience a decrease in *d*-excess by day-2. The mean is shifted to -1.2‰ over a 2-day period with decreases in *d*-excess documented in 45 out of the 60 samples (75%) during precipitation-free periods with minimal

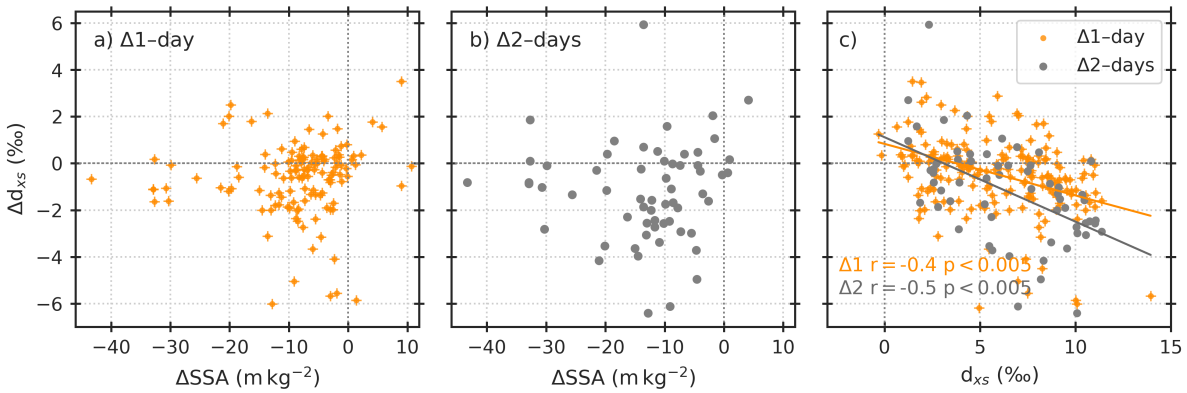

Figure 5. Isotopic changes during all the analysed events are shown, with each point indicating a specific sampling site. The daily change in *d*-excess (d_{xs}) and SSA is presented in a), change in *d*-excess and SSA over the first 2-days of each event is shown in b), and the respective changes in *d*-excess are plotted against the absolute *d*-excess values in c). Linear regressions are included for daily change (orange) and 2-day change (grey).

surface perturbation. Initial *d*-excess is observed to have a significant influence on the magnitude of *d*-excess decrease over the defined period (Fig. 5c), with high initial *d*-excess corresponding to the largest decreases in *d*-excess.

3.3.2 Low-wind event analysis

The following section focuses on latent heat fluxes and near-surface temperature gradients corresponding to isotopic change during low-wind events only. This is to ensure that surface layer we are analysing is constant throughout the event to avoid inaccurate interpretation of isotopic change. As mentioned in Section 3.2, ground fog preceded the SSA peak in E11, concur-

Table 3. Table of isotopic change for decay events. Mean values on day-0 and day-2 of each event, and percentage change over this 2-day period are presented for δ^{18}O, *d*-excess and SSA. Low-wind events (bold text) and moderate-wind events are presented.

	$\delta^{18}O$ (‰)			*d*-excess (‰)			SSA ($m^2\,kg^{-1}$)		
	Initial	Day-2	2-Day %Δ	Initial	Day-2	2-Day %Δ	Initial	Day-2	2-Day %Δ
E1	-34.72	-34.60	0.4%	5.0	4.5	-10.0%	51.3	33.9	-34.0%
E10	**-31.08**	**-30.56**	**1.7%**	**8.4**	**5.6**	**-33.3%**	**56.0**	**36.3**	**-35.1%**
E11	**-29.93**	**-29.95**	**-0.1%**	**5.5**	**4**	**-27.3%**	**45.3**	**28.6**	**-36.9%**
E13	-29.13	-29.10	0.1%	3.3	3.8	15.2%	54.1	36.6	-32.3%
E18	-24.08	-23.80	1.2%	11.4	7.8	-31.6%	65.3	37.2	-43.0%
E19	-23.40	-23.31	0.4%	6.7	6.8	1.5%	47.7	29.4	-38.2%

rent with negligible accumulation recorded. In contrast, almost 1 cm of snow was accumulated during the day prior to E10, corresponding to observation of snowfall.

Figure 6 shows the relationship between the daily change in isotopic composition for E10 and E11 (Δd-excess and $\Delta\delta^{18}$O) and SSA (ΔSSA). During E10, significant inverse correlations are observed between $\Delta\delta^{18}$O and Δd-excess, and between ΔSSA and Δd-excess (r=-0.5, r=-0.8), while $\Delta\delta^{18}$O and ΔSSA are positively correlated (r=0.6). In contrast, no significant relationship is observed between the Δ-parameters during E11, where there is negligible change in surface snow δ^{18}O (<0.7‰).

The direction of vapour fluxes are inferred using temperature gradients determined from air, surface and subsurface (10 cm depth) temperature data, and LE, measured as an upwards flux. Net-sublimation is observed during both E10 and E11, with a total sum of 33.9 W m^{-2} and 55.8 W m^{-2} for the respective events. LE is inversely related to the temperature gradient (TG) between the air and the surface, with strong sublimation (>10 W m^{-2}), corresponding to a negative TG of 2.5°C between the air and surface on June 10th. A concurrent upwards vapour flux is observed between the subsurface and surface, most apparent on June 11th (Day-2 of E10).

Negative LE up to -4 W m^{-1} are documented each night corresponding to the transition from a negative to positive TG between the air and surface. Net-deposition was recorded between sampling on 9th June at 15:18 UTC and 10th June 10:40 UTC (first day of E10) corresponding to a decrease in δ^{18}O and d-excess. The subsequent day, characterised by net sublimation, had a large increase in δ^{18}O and a larger decrease in d-excess. Contrary to E10, E11 is characterised by a large decrease in d-excess and a small decrease in δ^{18}O, both concurrent with net-sublimation and strong negative surface-subsurface TG. The air-surface TG during E11 has a lower mean and reduced diurnal amplitude than E10 facilitating sublimation for a longer period.

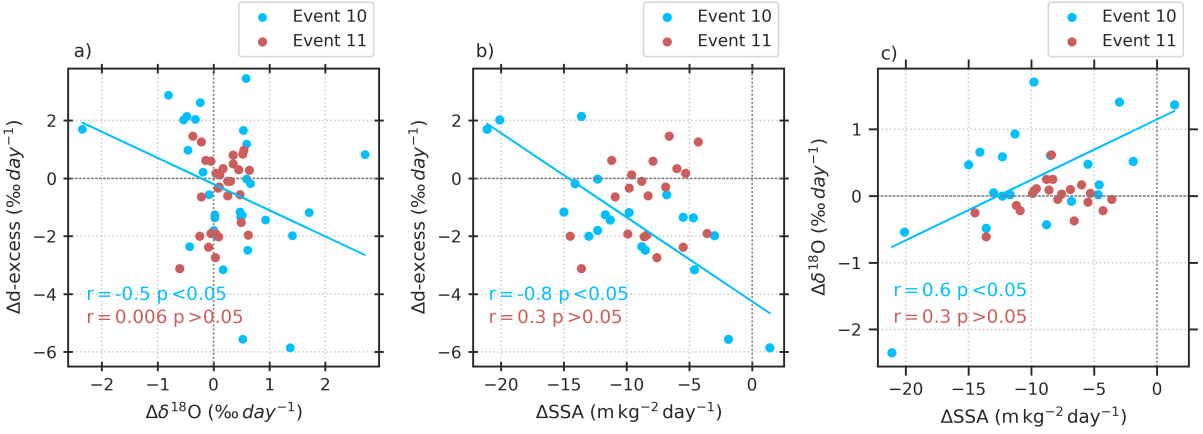

Figure 6. Isotopic change analysis for low-wind events, E10 and E11. Panel a) shows daily change in d-excess against change in δ^{18}O for E10 and E11, b) shows change in d-excess against change in SSA, and c) shows change in δ^{18}O and change in SSA. The r- and p-value for each regression are indicating in the corresponding colours. Only significant linear regressions are indicated with a line.

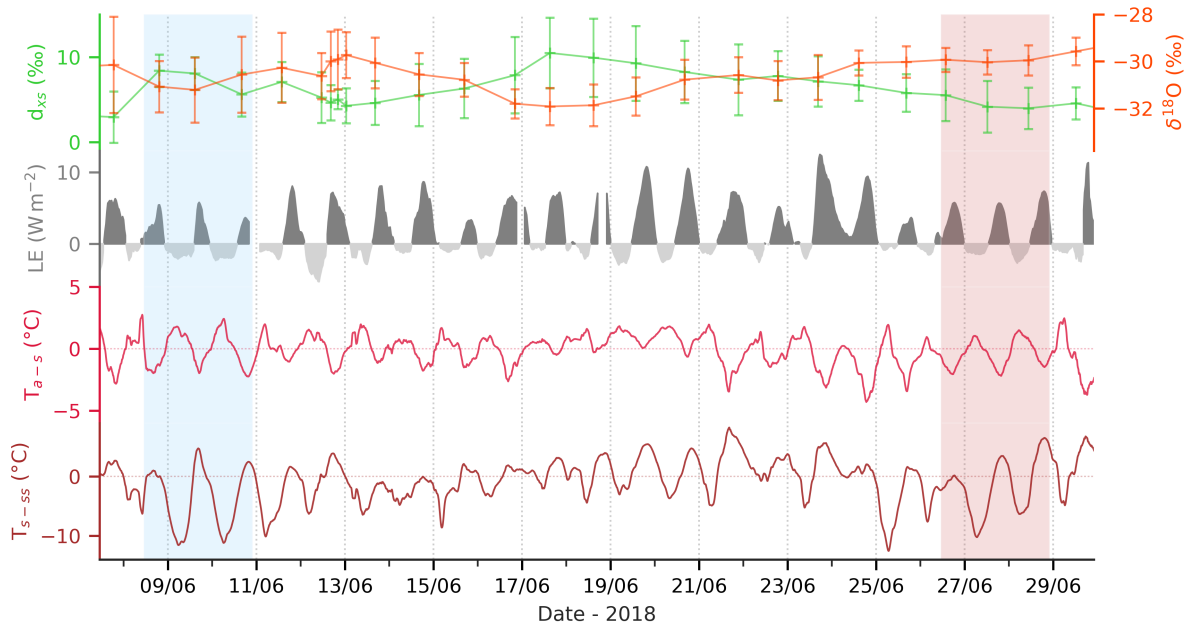

Figure 7. LE and temperature gradients for low-wind events. Latent heat flux (LE) (grey), air-surface temperature gradient (TG) (red) and surface-10 cm subsurface TG (red) during June 2018. E10 (blue) and E11 (red) are highlighted. Dark grey shading in LE indicates sublimation and light grey shows deposition.

4 Discussion

Continuous daily SSA measurements at EastGRIP during the summer season of 2017, 2018 and 2019 have allowed for quantification of variations in snow physical properties due to deposition and snow metamorphism. Understanding the relationship between rapid decreases in SSA and corresponding change in isotopic composition require clearly defined events and environmental context. Using a set of criteria, six SSA decay events during precipitation-free periods are defined and used to construct an empirical decay model with the decay rate tuned for low and moderate wind-speeds. We firstly discuss the behaviour of SSA decay at EastGRIP and compare to existing models. The isotopic change associated with low-wind SSA decay events is then considered, in the context of sublimation, interstitial diffusion and wind effects (Ebner et al., 2017; Hughes et al., 2021). Results from EOF analysis are used in combination with the isotopic change during SSA decay.

4.1 SSA decay at EastGRIP

Events of rapid SSA decay at EastGRIP are best described by an exponential decay function, in agreement with observations from Cabanes et al. (2003). No cold events (< -20 °C) are captured within the event criteria, potentially indicating 1) a need for warmer temperatures to induce such change in SSA over the time-period, or 2) that the local synopticity favours precipi-

tation coincident with low temperature and high winds during the summer. Within this framework, the events captured by the threshold with mean temperatures below -20 °C are likely capturing wind-erosion, exposing sub-surface snow with lower SSA.

The narrow temperature range of SSA decay events does not facilitate a conclusive definition of a temperature-dependent decay rate (Cabanes et al., 2003; Legagneux et al., 2003; Flanner and Zender, 2006; Taillandier et al., 2007). We instead assess the influence of wind-speed on the SSA decay rate and observe a more rapid SSA decay with increased wind-speed, which can be explained by increased ventilation of saturated pore air acting as a catalyst for snow metamorphism (Cabanes et al., 2003; Flanner and Zender, 2006; Neumann and Waddington, 2004).

Unsurprisingly, given the parameters are fit to the data, the model defined in the study predicts SSA decay for the low- and moderate-wind events with the lowest RMSE. The decay model from Taillandier et al. (2007) (T07) performed well. performed well for the moderate-wind events, but underestimated the rate of decay for the low-wind events. T07 was defined based on the SSA decay of fresh snow with densities below $180\,\mathrm{kg\,m^{-3}}$ (Taillandier et al., 2007), compared to a mean density of $266\,\mathrm{kg\,m^{-3}}$ for all low- and moderate-wind events in this study. The tendency for T07 to underestimate the SSA decay seems counter-intuitive given the possibility of aged snow in our study, which would plausibly be expected to experience SSA decay at a slower rate that fresh snow (Domine et al., 2007). In contrast, the model from Flanner and Zender (2006) (FZ06) consistently overestimates the observed SSA decay rate, most pronounced in E10 and E18. The original parameter values τ and n were tuned to data from alpine regions, potentially explaining the poor fit.

The simple empirical model presented here is limited to conditions at EastGRIP within a narrow temperature range and therefore is likely to be unsuitable for sites with different conditions. However, large errors when using the models from the literature indicate that the low-latitude tuning is not optimal for predicting surface snow SSA decay at EastGRIP.

4.2 Isotopic change during SSA decay events

4.2.1 Low-wind events

Three key mechanisms are expected to drive the rapid SSA decays, 1) large grains growing at the expense of small grains (Legagneux et al., 2004; Flanner and Zender, 2006), 2) diffusion of interstitial water vapour (Colbeck, 1983; Ebner et al., 2017; Touzeau et al., 2018), 3) sublimation reducing the dendricity of snow grains which is intensified by wind ventilating the saturated pore air, known as 'wind-pumping' (Neumann and Waddington, 2004). The dominant mechanisms can theoretically be identified by a combination of the change in isotopic composition - indicating the fractionation effect - and the LE and temperature gradient data to determine the direction of flux.

In theory, mechanism 1) causes minimal change in the bulk isotopic composition of a snow layer under isothermal conditions (Ebner et al., 2017). During no SSA decay events did the snow isotopic composition remain consistent. In the case of 2), interstitial diffusion, light isotopes are preferentially diffused, while the heavy isotopes will be preferentially deposited onto the cold snow grains (Colbeck, 1983; Ebner et al., 2017; Touzeau et al., 2016). Thus, diffusion of water vapour in the pore space causes a decrease in *d*-excess and slight increases in δ^{18}O due to kinetic fractionation (Flanner and Zender, 2006). Similarly, mechanism 3), sublimation, is widely documented to cause an increase in δ^{18}O of the remaining snow-mass due to isotopic

fractionation, and a significant decrease in *d*-excess expected to be due to kinetic fractionation (Ritter et al., 2016; Madsen et al., 2019; Hughes et al., 2021; Wahl et al., 2021; Casado et al., 2021). Conclusively identifying these mechanisms requires water vapour isotopes to model the fractionation effects. In the absence of this data, we infer potential explanations for isotopic change during the low-wind events.

An overall increase in δ^{18}O and decrease in *d*-excess during E10 is likely attributed to a combination of 2) and 3) based on observation of net-sublimation and high amplitude diurnal temperature gradient variability, indicating vapour transport within the pore space. The period between 9th June at 15:18 UTC and 10th June 10:40 UTC had net deposition corresponding to an overall decrease in δ^{18}O during the first day and minimal decrease in *d*-excess. An increase in snow δ^{18}O would be expected during deposition (Stenni et al., 2016; Feher et al., 2021; Casado et al., 2021), however, disequilibrium between water vapour isotopic composition and snow isotopic composition may explain the decrease in δ^{18}O (Wahl et al., 2021).

Both δ^{18}O and *d*-excess vary continuously throughout June 2018 (Fig. 7), with no clear relationship to total LE or temperature gradients. Strong diurnal surface and subsurface temperature gradients during the low-wind events can explain rapid SSA decay (Pinzer et al., 2012). We conclude that SSA of the surface snow is strongly influenced by surface-subsurface TG while the changes in isotopic composition are likely to be influenced by other factors such as the magnitude of vapour-snow isotopic disequilibrium during sublimation (Steen-Larsen et al., 2014; Hughes et al., 2021; Wahl et al., 2021). Decoupling the influence of sublimation and interstitial diffusion within the snow requires additional measurements of isotopic composition of atmospheric water vapour to model associated fractionation effects (Wahl et al., 2021). Our results suggest that while processes driving SSA decay (snow metamorphism) do modify the isotopic composition of the surface snow, interstitial diffusion has a disproportionate effect on SSA decay.

4.2.2 Inter-annual variability

The recurring difference in snow characteristics and temperature conditions during 2019 compared to 2017 and 2018 could be explained by the shifting phase of the North Atlantic Oscillation (NAO) which is in positive phase during 2018 and 2017 (below-average temperatures), and negative phase during 2019. A similar pattern is observed in the snow isotopes when considering the period between 27th May to 1st August where the mean $\delta^{18}O$ values during 2019 was -27.3‰, which is 4.3‰ higher than 2018 (-31.6‰) and 3.6‰ higher than 2017 (-30.9‰). While the difference in mean $\delta^{18}O$ can plausibly be explained by a 3.2°C mean air temperature difference, the isotope-SSA covariance is not so straightforward.

The positive mode of $\mathrm{PC1_{SSA}}$ can be interpreted as increases in SSA from depositional events, such as precipitation, surface hoar formation, and wind-fragmented snowdrift (Domine et al., 2009), while the negative mode is associated with snow metamorphism or wind-erosion (Cabanes et al., 2002, 2003; Legagneux et al., 2003, 2004; Taillandier et al., 2007; Flanner and Zender, 2006). Based on this interpretation, a covariance between $\mathrm{PC1_{SSA}}$ and $\mathrm{PC1}_{d\mathrm{xs}}$ or $\mathrm{PC1}_{\delta^{18}\mathrm{O}}$ indicates that the mechanisms controlling SSA variability also influence the isotopic composition.

We observe a decoupling of the temporal variance in *d*-excess from that of δ^{18}O (Fig. 3) in 2019 which is can be attributed to the *d*-excess signal being more sensitive to kinetic effects during sublimation and grain growth between pore air water vapour and the snow grains (Ebner et al., 2017; Casado et al., 2021).

Ongoing work to decouple the processes driving change in isotopic composition - sublimation from surface or interstitial vapour diffusion between layers in the pore space - is vital for precise climate reconstruction in ice cores (Touzeau et al., 2018; Hughes et al., 2021; Wahl et al., 2021; Casado et al., 2021). Future studies would benefit from obtaining direct measurements of the isotopic composition of precipitation and surface hoar, to determine the fraction of such deposits in the SSA samples. Furthermore, a quantitative representation of vapour fluxes in the surface snow rather than the temperature-gradient based approximation used in this study would provide a basis from which to quantify the relative influence of fractionation during sublimation and interstitial diffusion.

4.3 Implications and perspectives

Documented changes in snow isotopic composition during surface snow metamorphism have potential implications for interpretation of stable water isotope records from ice cores, given that the current interpretation assumes the precipitation signal is preserved (Dansgaard, 1964). Variations of d-excess in ice core records are attributed to changes in source region, source region conditions and kinetic fractionation occurring during snow crystal formation in supersaturated clouds (Stenni et al., 2010; Jouzel and Merlivat, 1984). However, we show that there are substantial changes in d-excess during precipitation-free periods supporting recent work showing that post-depositional factors add complexity to the traditional interpretation of ice core water isotope records. Greenland ice core d-excess records show abrupt decreases in d-excess corresponding to warming transitions, which is attributed to change in moisture source regions (Steffensen et al., 2008). Results presented in our study document decreases in snow d-excess during surface snow metamorphism associated with temperature gradients and sublimation, potentially contributing to the total decrease observed in the d-excess records.

The findings of this exploratory study reiterate the importance of quantifying the isotopic fractionation effects associated with processes driving snow metamorphism during precipitation-free periods. Moreover, the inter-annual variability observed at EastGRIP between 2018 and 2019 suggests that precipitation intermittency and temperature (gradients) play a role in isotopic change, which is not readily identified in the surface snow SSA data.

5 Conclusions

This study addresses the rapid SSA decay driven by surface snow metamorphism. In particular, the study aims to explore how rapid SSA decay relates to changes in isotopic composition of the surface snow in the dry accumulation zone of the Greenland Ice Sheet. Ten individual snow samples were collected daily over a 90 m transect at EastGRIP in the period between May and August of 2017, 2018 and 2019. SSA and isotopic composition were measured for each sample. Periods of snow metamorphism after deposition events were defined using SSA measurements to extract periods of rapid decreases in SSA.

An exponential SSA decay model ($SSA(t) = (SSA_0 - 22) \cdot e^{-\alpha \cdot t} + 22$) was constructed to describe surface snow metamorphism in summer conditions for polar snow, with surface temperatures above -20 °C and with minimal surface perturbation. Two event categories were defined based on wind speed, with an upper threshold of $7\,\mathrm{m\,s^{-1}}$ to minimise chance of snowdrift.

Wind speed is observed to increase surface SSA decay rate showing that snow metamorphism is enhanced with increased ventilation.

Changes in isotopic composition corresponding to post-depositional processes driving SSA decay are observed in all low- and moderate-wind events. A decrease in d-excess from day-0 to day-2 is observed in 4 out of the 6 events with no precipitation. Further analysis of low-wind SSA decay events indicates that the combined effects of vapour diffusion and diurnal LE variability causes isotopic fractionation of the surface snow in the absence of precipitation. The differing fractionation effects are expected to be the result of vapour-snow isotopic disequilibrium. A strong correlation observed between SSA and d-excess found in 2019 was not present for 2018. We suggest that this is due to strong sublimation corresponding to high temperatures during 2019.

In summary, our results support documentation of fractionation during sublimation and deposition between the snow surface and atmosphere, indicating that the precipitation isotopic composition signal is not always preserved during the processes driving surface snow metamorphism. Observations of post-depositional decrease in d-excess during rapid SSA decay hints to local processes influencing the d-excess signal and therefore an interpretation as source region signal alone is insufficient.

Appendix A

Table A1. Description of conditions for SSA decays captured by decrease threshold. Duration and conditions for all 21 events defined by the threshold. Observations were made of snowfall, snowdrift and ground fog. Presented here are the conditions during the day (24h) preceding each event (Initial conditions), the dominant conditions throughout the event (Sky conditions) and observations of surface perturbations (Comments). based on field observations.

	Date	Event No.	Surface temp. (°C)	Initial conditions	Sky conditions	Comments
2017	27/05 - 31/05	E1	-17.3	No clear driver	Clear-sky	
	19/06 - 24/06	E2	-13.6	Snowfall	Clear-sky	Fog
	30/06 - 02/07	E3	-14.0	Snowfall	Overcast	Snowdrift
	10/07 - 15/07	E4	-13.2	Snowfall	Clear-sky	Fog and snowfall
	18/07 - 19/07	E5	-11.7	Snowfall	Overcast	Snowdrift
	21/07 - 23/07	E6	-11.2	Snowfall	Overcast	Snowdrift
2018	07/05 - 10/05	E7	-33.7	Drift and fog	Clear/ice-fog	Fog
	14/05 - 15/05	E8	-19.8	Snowfall	Clear-sky	Fog and snowfall
	16/05 - 18/05	E9	-21.5	Snowfall and fog	Overcast	Fog and snowfall
	09/06 - 11/06	E10	-14.9	Snowfall	Overcast	
	27/06 - 29/06	E11	-15.3	Ground fog	Clear-sky	
	30/06 - 03/07	E12	-11.2	Wind drifted snow	Clear-sky	Snowfall
	04/07 - 06/07	E13	-10.2	Snowfall	Clear-sky	
	16/07 - 21/07	E14	-14.3	No clear driver	Clear-sky	Fog and snowfall
	23/07 - 27/07	E15	-14.1	Ground fog	Clear-sky	
2019	17/06 - 20/06	E16	-11.4	Snowfall	Clear-sky	Snowfall
	27/06 - 30/06	E17	-9.5	No clear driver	Overcast	Fog and snowfall
	02/07 - 05/07	E18	-7.0	Snowfall	Overcast	
	06/07 - 08/07	E19	-10.0	No clear driver	Clear-sky	
	18/07 - 20/07	E20	-7.6	Ground fog	Overcast	
	28/07 - 31/07	E21	-6.5	No clear driver	Clear-sky	

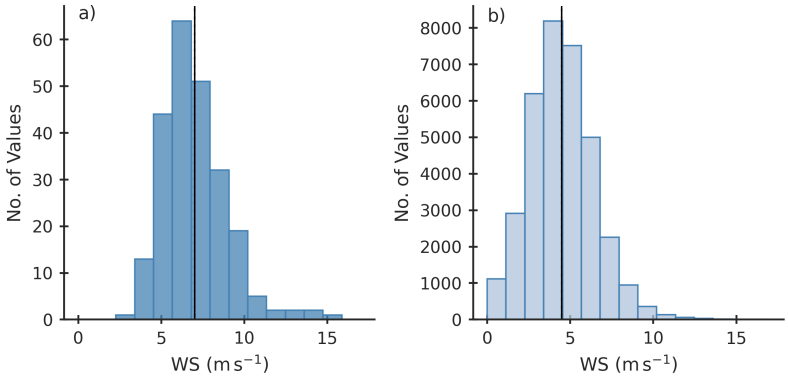

Figure A1. *Wind-speed Distribution*

Histograms showing a) the daily maximum values and b) the 10-minute mean values for all sampling days of 2017, 2018 and 2019. The black line indicates the mean.

Data availability. The SSA, density and accumulation data for all sampling years is available on the PANGAEA database with the DOI:***. Snow isotope data is also available on the PANGAEA database with the DOI:***. Data from the Programme for Monitoring of the Greenland Ice Sheet (PROMICE) 400 were provided by the Geological Survey of Denmark and Greenland (GEUS) at http://www.promice.dk. Eddy Covaraniance Tower measurement are available on the PANGAEA database with the DOI: https://doi.org/10.1594/PANGAEA.928827.

Author contributions. HCSL, AKF and RHS designed the study together. AKF, SW, MH, MB, AZ, SK and HCSL carried out the data collection and measurements. RHS, AKF and HCSL worked directly with the data. RHS, AKF and HCSL prepared the manuscript with contributions from all co-authors. AKF contributed largely to the manuscript text and structure. HCSL designed and administrated the SNOWISO project.

Competing interests. The authors declare that they have no conflict of interest.

Acknowledgements. This project has received funding from the European Research Council (ERC) under the European Union's Horizon 2020 research and innovation program: Starting Grant-SNOWISO (grant agreement 759526). EastGRIP is directed and organized by the Centre for Ice and Climate at the Niels Bohr Institute, University of Copenhagen. It is supported by funding agencies and institutions in Denmark (A. P. Møller Foundation, University of Copen-hagen), USA (US National Science Foundation, Office of Polar Programs), Germany (Alfred Wegener Institute, Helmholtz Centre for Polar and Marine Research), Japan (National Institute of Polar Research and Arctic Challenge for Sustainability), Norway (University of Bergen and Bergen Research Foun-dation), Switzerland (Swiss National Science

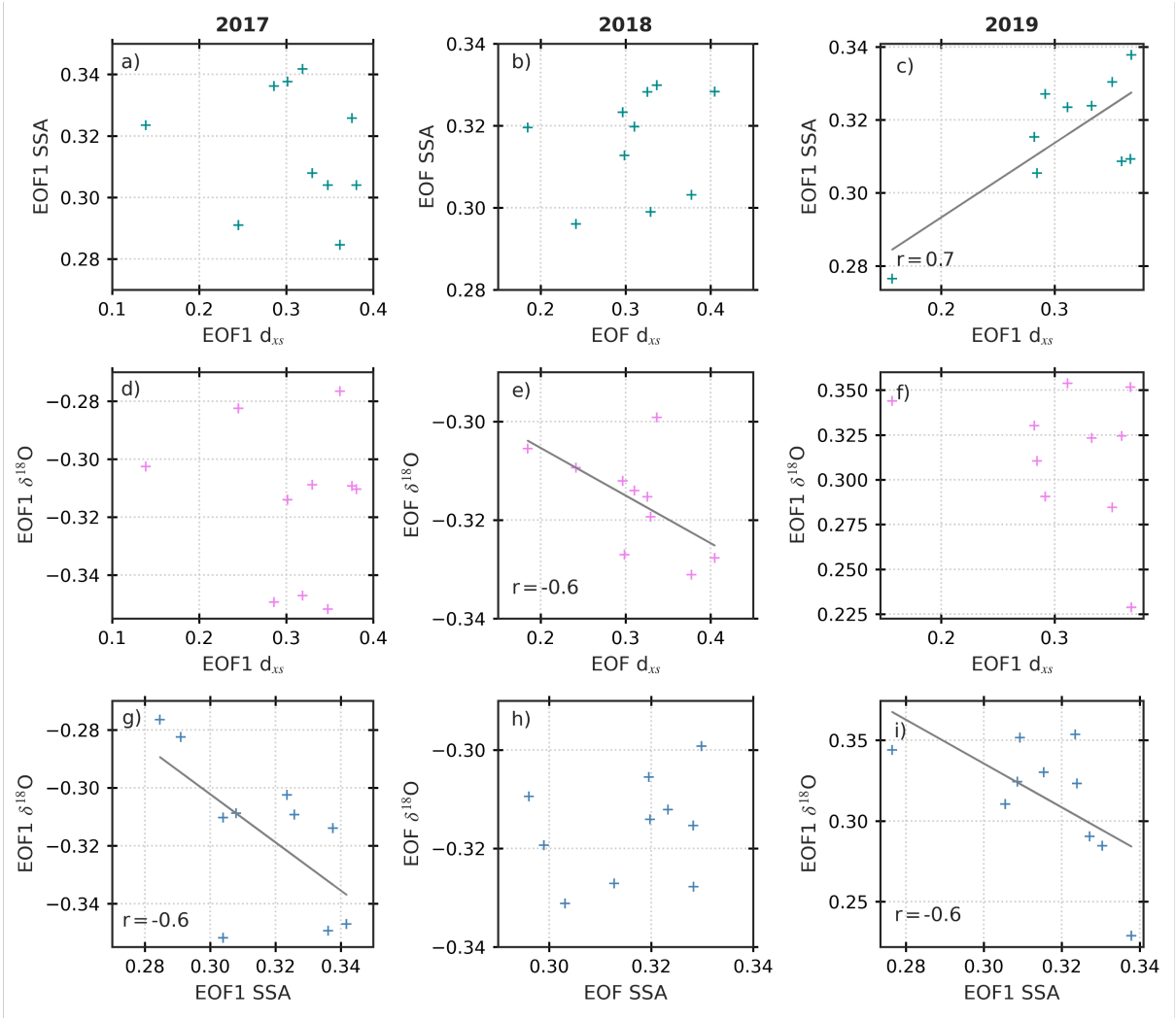

Figure A2. Results from the EOF analysis showing the relationship between SSA, *d*-excess and δ^{18}O in the spatial dimension. Linear regressions are included in plots with significant correlations ($p<0.05$) between variables.

Foundation), France (French Polar Institute Paul-Emile Victor, Insti-tute for Geosciences and Environmental research), and China (Chinese Acad-emy of Sciences and Beijing Normal University).

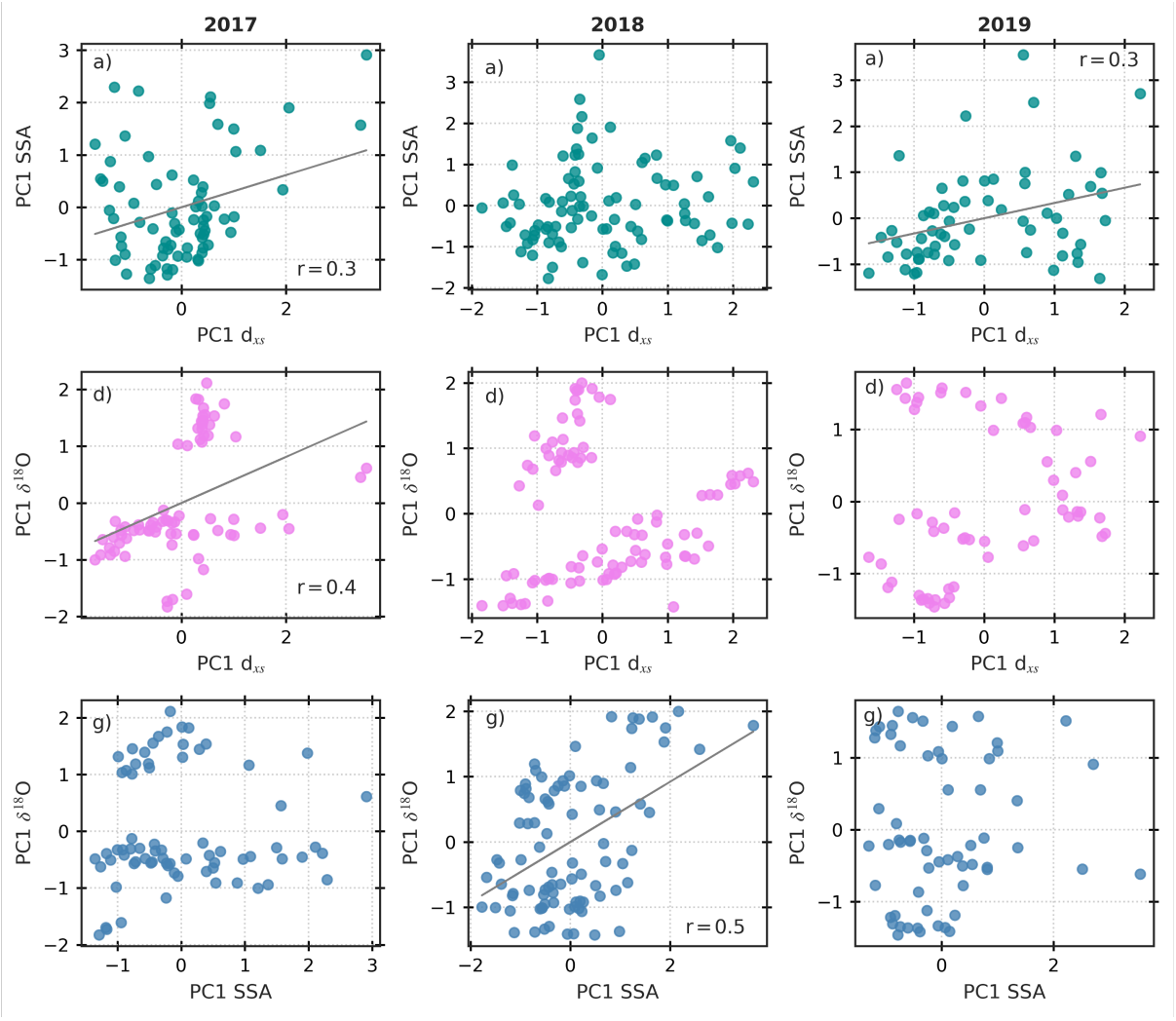

Figure A3. Results from the EOF analysis showing the relationship between SSA, *d*-excess and δ^{18}O in the temporal dimension. Linear regressions are included in plots with significant correlations ($p<0.05$) between variables.

References

Birnbaum, G., Freitag, J., Brauner, R., Ko¨nig, G., Ko¨nig-Langlo, K., Schulz, E., Kipfstuhl, S., Oerter, H., Reijmer, C. H., Schlosser, E., Faria, S. H., Ries, H., Loose, B., Herber, A., Duda, M. G., Powers, J. G., Manning, K. W., and Van Den Broeke, M. R.: Strong-wind events and their influence on the formation of snow dunes: observations from Kohnen station, Dronning Maud Land, Antarctica, Journal of Glaciology, 56, 891–902, https://www.cambridge.org/core., 2010.

Cabanes, A., Legagneux, L., and Dominé, F.: Evolution of the specific surface area and of crystal morphology of Arctic fresh snow during the ALERT 2000 campaign, Atmospheric Environment, 36, 2767–2777, https://doi.org/10.1016/S1352-2310(02)00111-5, 2002.

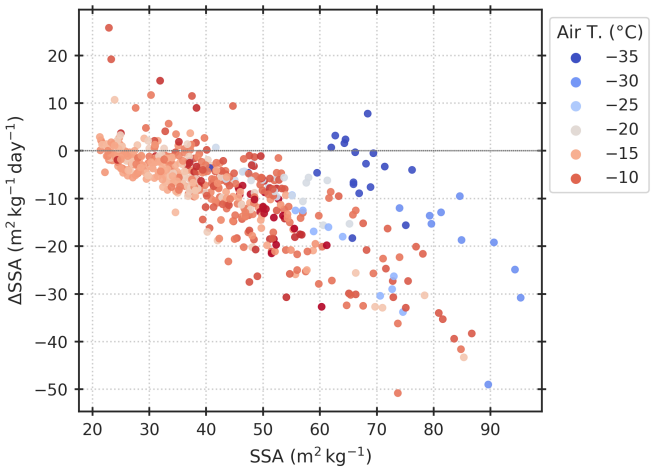

Figure A4. The derivative of SSA is shown as a function of SSA. All events captured by the decrease threshold are included here. The markers are coloured by mean air temperature between sampling.

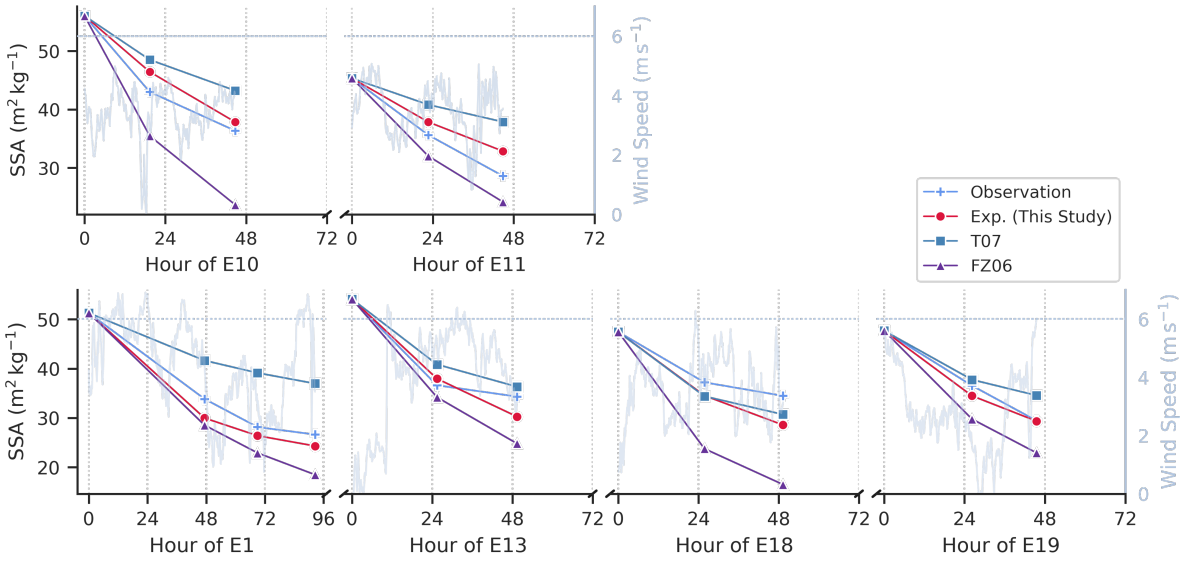

Figure A5. SSA decay model evaluation and a comparison to observations. Included models are the decay model from this study and the existing decay models from Flanner and Zender (2006), FZ06, and Taillandier et al. (2007), T07. The 10-minute averaged wind-speed is shown on the secondary y-axis, with the $6\,m^2\,kg^{-1}$ thresholds indicated. Low-wind events E10 and E11 are shown in the upper panel, and moderate-wind events are shown in the lower panel (E1, E13, E18 and E19).

Cabanes, A., Legagneux, L., and Dominé, F.: Rate of evolution of the specific surface area of surface snow layers, Environmental Science and Technology, 37, 661–666, https://doi.org/10.1021/es025880r, 2003.

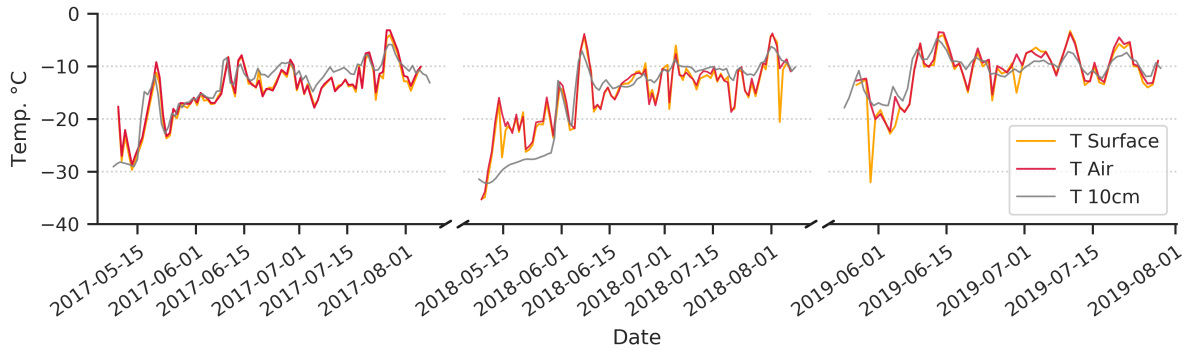

Figure A6. Daily mean air, surface and subsurface temperature time-series for 2017, 2018 and 2019.

Carmagnola, C. M., Domine, F., Dumont, M., Wright, P., Strellis, B., Bergin, M., Dibb, J., Picard, G., Libois, Q., Arnaud, L., and Morin, S.: Snow spectral albedo at Summit, Greenland: Measurements and numerical simulations based on physical and chemical properties of the snowpack, Cryosphere, 7, 1139–1160, https://doi.org/10.5194/tc-7-1139-2013, 2013.

Casado, M., Landais, A., Picard, G., Münch, T., Laepple, T., Stenni, B., Dreossi, G., Ekaykin, A., Arnaud, L., Genthon, C., Touzeau, A., Masson-Delmotte, V., and Jouzel, J.: Archival processes of the water stable isotope signal in East Antarctic ice cores, Cryosphere, 12, 1745–1766, https://doi.org/10.5194/tc-12-1745-2018, 2018.

Casado, M., Münch, T., and Laepple, T.: Climatic information archived in ice cores: Impact of intermittency and diffusion on the recorded isotopic signal in Antarctica, Climate of the Past, 16, 1581–1598, https://doi.org/10.5194/cp-16-1581-2020, 2020.

Casado, M., Landais, A., Picard, G., Arnaud, L., Dreossi, G., Stenni, B., and Prié, F.: Water Isotopic Signature of Surface Snow Metamorphism in Antarctica, Geophysical Research Letters, 48, https://doi.org/10.1029/2021GL093382, 2021.

Christiansen, H. H.: Snow-cover depth, distribution and duration data from northeast Greenland obtained by continuous automatic digital photography, Annals of Glaciology, 32, 102–108, https://www.cambridge.org/core., 2001.

Ciais, P. and Jouzel, J.: Deuterium and oxygen 18 in precipitation: Isotopic model, including mixed cloud processes, Tech. Rep. D8, 1994.

Colbeck, S. C.: Thermodynamics of snow metamorphism due to variations in curvature, Journal of Glaciology, 26, 291–301, https://www.cambridge.org/core., 1980.

Colbeck, S. C.: Theory of metamorphism of dry snow., Journal of Geophysical Research, 88, 5475–5482, https://doi.org/10.1029/JC088iC09p05475, 1983.

Dansgaard, W.: Stable isotopes in precipitation, Tellus, 16, 436–468, https://doi.org/10.3402/tellusa.v16i4.8993, 1964.

Domine, F., Taillandier, A. S., and Simpson, W. R.: A parameterization of the specific surface area of seasonal snow for field use and for models of snowpack evolution, Journal of Geophysical Research: Earth Surface, 112, 1–13, https://doi.org/10.1029/2006JF000512, 2007.

Domine, F., Taillandier, A. S., Cabanes, A., Douglas, T. A., and Sturm, M.: Three examples where the specific surface area of snow increased over time, Cryosphere, 3, 31–39, https://doi.org/10.5194/tc-3-31-2009, 2009.

Ebner, P. P., Steen-Larsen, H. C., Stenni, B., Schneebeli, M., and Steinfeld, A.: Experimental observation of transient δ18O interaction between snow and advective airflow under various temperature gradient conditions, The Cryosphere Discussions, pp. 1–36, https://doi.org/10.5194/tc-2017-16, 2017.

Faber, A. K., Vinther, B. M., Sjolte, J., and Pedersen, R. A.: How does sea ice influence δ18O of Arctic precipitation?, Atmospheric Chemistry and Physics, 17, 5865–5876, https://doi.org/10.5194/acp-17-5865-2017, 2017.

Fausto, R. S., Van As, D., Mankoff, K. D., Vandecrux, B., Citterio, M., Ahlstrøm, A. P., Andersen, S. B., Colgan, W., Karlsson, N. B., Kjeldsen, K. K., Korsgaard, N. J., Larsen, S. H., Nielsen, S., Pedersen, A. , Shields, C. L., Solgaard, A. M., and Box, J. E.: PROMICE automatic weather station data, Earth System Science Data, 80, 1–41, https://doi.org/10.22008/promice/data/aws, 2021.

Feher, R., Voiculescu, M., Chiroiu, P., and Perșoiu, A.: The stable isotope composition of hoarfrost, https://doi.org/10.1080/10256016.2021.1917567, 2021.

Flanner, M. G. and Zender, C. S.: Linking snowpack microphysics and albedo evolution, Journal of Geophysical Research Atmospheres, 111, 1–12, https://doi.org/10.1029/2005JD006834, 2006.

Flin, F. and Brzoska, J. B.: The temperature-gradient metamorphism of snow: Vapour diffusion model and application to tomographic images, Annals of Glaciology, 49, 17–21, https://doi.org/10.3189/172756408787814834, 2008.

Gallet, J. C., Domine, F., Zender, C. S., and Picard, G.: Measurement of the specific surface area of snow using infrared reflectance in an integrating sphere at 1310 and 1550 nm, Cryosphere, 3, 167–182, https://doi.org/10.5194/tc-3-167-2009, 2009.

Gallet, J. C., Domine, F., Arnaud, L., Picard, G., and Savarino, J.: Vertical profile of the specific surface area and density of the snow at Dome C and on a transect to Dumont D'Urville, Antarctica - Albedo calculations and comparison to remote sensing products, Cryosphere, 5, 631–649, https://doi.org/10.5194/tc-5-631-2011, 2011.

Gallet, J. C., Domine, F., Savarino, J., Dumont, M., and Brun, E.: The growth of sublimation crystals and surface hoar on the Antarctic plateau, Cryosphere, 8, 1205–1215, https://doi.org/10.5194/tc-8-1205-2014, 2014.

Genthon, C., Piard, L., Vignon, E., Madeleine, J. B., Casado, M., and Gallée, H.: Atmospheric moisture supersaturation in the near-surface atmosphere at Dome C, Antarctic Plateau, Atmospheric Chemistry and Physics, 17, 691–704, https://doi.org/10.5194/acp-17-691-2017, 2017.

Holme, C., Gkinis, V., and Vinther, B. M.: Molecular diffusion of stable water isotopes in polar firn as a proxy for past temperatures, Geochimica et Cosmochimica Acta, 225, 128–145, https://doi.org/10.1016/j.gca.2018.01.015, 2018.

Hughes, A. G., Wahl, S., Jones, T. R., Zuhr, A., Hörhold, M., White, J. W. C., and Steen-Larsen, H. C.: The role of sublimation as a driver of climate signals in the water isotope content of surface snow: Laboratory and field experimental results, The Cryosphere, https://doi.org/10.5194/tc-2021-87, 2021.

Johnsen, S. ., Clausen, H. B., Cuffey, K. M., Hoffmann, G., Schwander, J., and Creyts, T.: Diffusion of stable isotopes in polar firn and ice: the isotope effect in firn diffusion, Physics of Ice Core Records, pp. 121–142, 2000.

Johnsen, S. J., Dansgaard, W., and White, J. W.: The origin of Arctic precipitation under present and glacial conditions, Tellus, Series B, 41 B, 452–468, https://doi.org/10.3402/tellusb.v41i4.15100, 1989.

Jouzel, J. and Merlivat, L.: Deuterium and oxygen 18 in precipitation: modeling of the isotopic effects during snow formation., Journal of Geophysical Research, 89, 749–757, https://doi.org/10.1029/jd089id07p11749, 1984.

Klein, K.: Variability in dry Antarctic firn - Investigations on spatially distributed snow and firn samples from Dronning Maud Land, Antarctica, PhD Thesis, University of Bremen, 3, 1–15, https://doi.org/10.1016/j.cell.2009.01.043, 2014.

Laepple, T., Münch, T., Casado, M., Hoerhold, M., Landais, A., and Kipfstuhl, S.: On the similarity and apparent cycles of isotopic variations in East Antarctic snow pits, Cryosphere, 12, 169–187, https://doi.org/10.5194/tc-12-169-2018, 2018.

Landais, A., Barnola, J. M., Kawamura, K., Caillon, N., Delmotte, M., Van Ommen, T., Dreyfus, G., Jouzel, J., Masson-Delmotte, V., Minster, B., Freitag, J., Leuenberger, M., Schwander, J., Huber, C., Etheridge, D., and Morgan, V.: Firn-air δ15N in modern polar

sites and glacial-interglacial ice: A model-data mismatch during glacial periods in Antarctica?, Quaternary Science Reviews, 25, 49–62, https://doi.org/10.1016/j.quascirev.2005.06.007, 2006.

Legagneux, L. and Domine, F.: A mean field model of the decrease of the specific surface area of dry snow during isothermal metamorphism, Journal of Geophysical Research: Earth Surface, 110, https://doi.org/10.1029/2004JF000181, 2005.

Legagneux, L., Cabanes, A., and Dominé, F.: Measurement of the specific surface area of 176 snow samples using methane adsorption at 77 K, Journal of Geophysical Research Atmospheres, 107, 5–1, https://doi.org/10.1029/2001JD001016, 2002.

Legagneux, L., Lauzier, T., Dominé, F., Kuhs, W. F., Heinrichs, T., and Techmer, K.: Rate of decay of specific surface area of snow during isothermal experiments and morphological changes studied by scanning electron microscopy, Canadian Journal of Physics, 81, 459–468, https://doi.org/10.1139/p03-025, 2003.

Legagneux, L., Taillandier, A. S., and Domine, F.: Grain growth theories and the isothermal evolution of the specific surface area of snow, Journal of Applied Physics, 95, 6175–6184, https://doi.org/10.1063/1.1710718, 2004.

Li, L. and Pomeroy, J. W.: Estimates of threshold wind speeds for snow transport using meteorological data, Journal of Applied Meteorology, 36, 205–213, https://doi.org/10.1175/1520-0450(1997)036<0205:EOTWSF>2.0.CO;2, 1997.

Linow, S., Hörhold, M. W., and Freitag, J.: Grain-size evolution of polar firn: A new empirical grain growth parameterization based on X-ray microcomputer tomography measurements, Journal of Glaciology, 58, 1245–1252, https://doi.org/10.3189/2012JoG11J256, 2012.

Madsen, M. V., Steen-Larsen, H. C., Hörhold, M., Box, J., Berben, S. M., Capron, E., Faber, A. K., Hubbard, A., Jensen, M. F., Jones, T. R., Kipfstuhl, S., Koldtoft, I., Pillar, H. R., Vaughn, B. H., Vladimirova, D., and Dahl-Jensen, D.: Evidence of Isotopic Fractionation During Vapor Exchange Between the Atmosphere and the Snow Surface in Greenland, Journal of Geophysical Research: Atmospheres, 124, 2932–2945, https://doi.org/10.1029/2018JD029619, 2019.

Masson-Delmotte, V., Landais, A., Stievenard, M., Cattani, O., Falourd, S., Jouzel, J., Johnsen, S. J., Dahl-Jensen, D., Sveinsbjornsdottir, A., White, J. W., Popp, T., and Fischer, H.: Holocene climatic changes in Greenland: Different deuterium excess signals at Greenland Ice Core Project (GRIP) and NorthGRIP, Journal of Geophysical Research D: Atmospheres, 110, 1–13, https://doi.org/10.1029/2004JD005575, 2005.

Merlivat, L. and Jouzel, J.: Global climatic interpretation of the deuterium-oxygen 16 relationship for precipitation., Journal of Geophysical Research, 84, 5029–5033, https://doi.org/10.1029/JC084iC08p05029, 1979.

Neumann, T. A. and Waddington, E. D.: Effects of firn ventilation on isotopic exchange, Journal of Glaciology, 50, 183–194, https://www.cambridge.org/core., 2004.

Picard, G., Royer, A., Arnaud, L., and Fily, M.: Influence of meter-scale wind-formed features on the variability of the microwave brightness temperature around Dome C in Antarctica, Cryosphere, 8, 1105–1119, https://doi.org/10.5194/tc-8-1105-2014, 2014.

Picard, G., Arnaud, L., Caneill, R., Lefebvre, E., and Lamare, M.: Observation of the process of snow accumulation on the Antarctic Plateau by time lapse laser scanning, Cryosphere, 13, 1983–1999, https://doi.org/10.5194/tc-13-1983-2019, 2019.

Pinzer, B. and Schneebeli, M.: Temperature gradient metamorphism is not a classical coarsening process, ISSW 09 - International Snow Science Workshop, Proceedings, pp. 58–61, 2009.

Pinzer, B. R., Schneebeli, M., and Kaempfer, T. U.: Vapor flux and recrystallization during dry snow metamorphism under a steady temperature gradient as observed by time-lapse micro-tomography, Cryosphere, 6, 1141–1155, https://doi.org/10.5194/tc-6-1141-2012, 2012.

Ritter, F., Christian Steen-Larsen, H., Werner, M., Masson-Delmotte, V., Orsi, A., Behrens, M., Birnbaum, G., Freitag, J., Risi, C., and Kipfstuhl, S.: Isotopic exchange on the diurnal scale between near-surface snow and lower atmospheric water vapor at Kohnen station, East Antarctica, Cryosphere, 10, 1647–1663, https://doi.org/10.5194/tc-10-1647-2016, 2016.

Schaller, C. F., Freitag, J., and Eisen, O.: Critical porosity of gas enclosure in polar firn independent of climate, Climate of the Past, 13, 1685–1693, https://doi.org/10.5194/cp-13-1685-2017, 2017.

Sime, L. C., Risi, C., Tindall, J. C., Sjolte, J., Wolff, E. W., Masson-delmotte, V., and Capron, E.: Warm climate isotopic simulations : what do we learn about interglacial signals in Greenland ice cores ?, Quaternary Science Reviews, 67, 59–80, https://doi.org/10.1016/j.quascirev.2013.01.009, 2013.

Sodemann, H., Masson-Delmotte, V., Schwierz, C., Vinther, B. M., and Wernli, H.: Interannual variability of Greenland winter precipitation sources: 2. Effects of North Atlantic Oscillation variability on stable isotopes in precipitation, Journal of Geophysical Research Atmospheres, 113, 1–21, https://doi.org/10.1029/2007JD009416, 2008.

Sokratov, S. A. and Golubev, V. N.: Snow isotopic content change by sublimation, Journal of Glaciology, 55, 823–828, https://doi.org/10.3189/002214309790152456, 2009.

Steen-Larsen, H. C., Sveinbjörnsdottir, A. E., Peters, A. J., Masson-Delmotte, V., Guishard, M. P., Hsiao, G., Jouzel, J., Noone, D., Warren, J. K., and White, J. W.: Climatic controls on water vapor deuterium excess in the marine boundary layer of the North Atlantic based on 500 days of in situ, continuous measurements, Atmospheric Chemistry and Physics, 14, 7741–7756, https://doi.org/10.5194/acp-14-7741-2014, 2014.

Steffensen, J. P., Andersen, K. K., Bigler, M., Clausen, H. B., Dahl-Jensen, D., Fischer, H., Goto-Azuma, K., Hansson, M., Johnsen, S. J., Jouzel, J., Masson-Delmotte, V., Popp, T., Rasmussen, S. O., Röthlisberger, R., Ruth, U., Stauffer, B., Siggaard-Andersen, M. L., Sveinbjörnsdottir, E., Svensson, A., and White, J. W.: High-resolution greenland ice core data show abrupt climate change happens in few years, Science, 321, 680–684, https://doi.org/10.1126/science.1157707, 2008.

Stenni, B., Masson-Delmotte, V., Selmo, E., Oerter, H., Meyer, H., Röthlisberger, R., Jouzel, J., Cattani, O., Falourd, S., Fischer, H., Hoffmann, G., Iacumin, P., Johnsen, S. J., Minster, B., and Udisti, R.: The deuterium excess records of EPICA Dome C and Dronning Maud Land ice cores (East Antarctica), Quaternary Science Reviews, 29, 146–159, https://doi.org/10.1016/j.quascirev.2009.10.009, 2010.

Stenni, B., Scarchilli, C., Masson-Delmotte, V., Schlosser, E., Ciardini, V., Dreossi, G., Grigioni, P., Bonazza, M., Cagnati, A., Karlicek, D., Risi, C., Udisti, R., and Valt, M.: Three-year monitoring of stable isotopes of precipitation at Concordia Station, East Antarctica, Cryosphere, 10, 2415–2428, https://doi.org/10.5194/tc-10-2415-2016, 2016.

Taillandier, A. S., Domine, F., Simpson, W. R., Sturm, M., and Douglas, T. A.: Rate of decrease of the specific surface area of dry snow: Isothermal and temperature gradient conditions, Journal of Geophysical Research: Earth Surface, 112, 1–13, https://doi.org/10.1029/2006JF000514, 2007.

Touzeau, A., Landais, A., Stenni, B., Uemura, R., Fukui, K., Fujita, S., Guilbaud, S., Ekaykin, A., Casado, M., Barkan, E., Luz, B., Magand, O., Teste, G., Le Meur, E., Baroni, M., Savarino, J., Bourgeois, I., and Risi, C.: Acquisition of isotopic composition for surface snow in East Antarctica and the links to climatic parameters, Cryosphere, 10, 837–852, https://doi.org/10.5194/tc-10-837-2016, 2016.

Touzeau, A., Landais, A., Morin, S., Arnaud, L., and Picard, G.: Numerical experiments on vapor diffusion in polar snow and firn and its impact on isotopes using the multi-layer energy balance model Crocus in SURFEX v8.0, Geoscientific Model Development, 11, 2393–2418, https://doi.org/10.5194/gmd-11-2393-2018, 2018.

Van As, D.: Warming, glacier melt and surface energy budget from weather station observations in the Melville Bay region of northwest Greenland, Journal of Glaciology, 47, https://www.cambridge.org/core., 2011.

Van Geldern, R. and Barth, J. A.: Optimization of instrument setup and post-run corrections for oxygen and hydrogen stable isotope measurements of water by isotope ratio infrared spectroscopy (IRIS), Limnology and Oceanography: Methods, 10, 1024–1036, https://doi.org/10.4319/lom.2012.10.1024, 2012.

Vinther, B. M., Buchardt, S., Clausen, H., Dahl-Jensen, D., Johnsen, S., Fisher, D., Koerner, R., Raynaud, D., Lipenkov, V., Andersen, K., Blunier, T., Rasmussen, S., Steffensen, J., and Svensson, A.: Holocene thinning of the Greenland ice sheet, Nature, 461, 385–388, 2009.

Wahl, S., Steen-Larsen, H. C., and Reuder, J.: Quantifying the Stable Water Isotopologue Exchange between Snow Surface and Lower Atmosphere by Direct Flux Measurements, Journal of Geophysical Research: Atmospheres, https://doi.org/10.1029/2020jd034400, 2021.

Zuanon, N.: IceCube, a portable and reliable instrument for snow specific surface area measurement in the field, International Snow Science Workshop, pp. 1020–1023, www.A2PhotonicSensors.com, 2013.

Zuhr, A. M., Münch, T., Steen-Larsen, H. C., Hörhold, M., and Laepple, T.: Local-scale deposition of surface snow on the Greenland ice sheet, The Cryosphere, 15, 4873–4900, https://doi.org/10.5194/tc-15-4873-2021, 2021.